A&A, 714, A459 (2026)
https://doi.org/10.1051/0004-6361/202661354
© The Authors 2026

Astronomy & Astrophysics

The methanol–methyl cyanide correlation: A chemical path from protostars to comets

M. Lippi[1,⋆], L. Podio[1], M. Cordiner[2,8], C. Codella[1], C. Walsh[3], A. S. Booth[4], N. Biver[5], D. Bockelée-Morvan[5], L. Giani[1], C. Ceccarelli[6], S. Faggi[2,7], and G. L. Villanueva[2]

[1] INAF, Osservatorio Astrofisico di Arcetri, Largo E. Fermi 5, 50125 Firenze, Italy
[2] NASA – Goddard Space Flight Center, 8800 Greenbelt Rd, Greenbelt, MD 20771, USA
[3] School of Physics and Astronomy, University of Leeds, Leeds LS2 9JT, UK
[4] Center for Astrophysics, Harvard & Smithsonian, Cambridge, USA
[5] Observatoire de Paris, LESIA, Meudon, France
[6] Univ. Grenoble Alpes, CNRS, IPAG, 38000 Grenoble, France
[7] American University, 4400 Massachusetts Ave NW, Washington, DC 20016, USA
[8] Catholic University of America, Washington, DC, USA

Received 9 June 2026 / Accepted 29 August 2026

ABSTRACT

Context. Comets are the frozen remnants of the early Solar System. By investigating their chemical composition, we can unveil the physical processes that shaped our planetary system and the evolution of interstellar material into planetary building blocks.
Aims. Systematic comparisons of the chemical composition of protostellar environments, disks, and comets remain rare and are often restricted to a narrow selection of targets. This study overcomes these limitations by employing a broader statistical approach that allowed us to identify inconsistencies in existing datasets. It thus provides a more comprehensive overview.
Methods. We present the first statistical analysis of methyl cyanide (CH_3CN) and methanol (CH_3OH) across a diverse and consistent sample, including 13 comets, 24 low-mass hot corinos, and seven planet-forming disks. We focused on the [CH_3CN]/[CH_3OH] abundance ratio, which is strongly correlated in hot corinos and might provide a sensitive diagnostic of the thermal and chemical evolution from interstellar clouds to planetary building blocks.
Results. While the [CH_3CN]/[CH_3OH] abundance ratios vary significantly within the planet-forming disk sample, this ratio is remarkably similar in comets and hot corinos. This indicates that despite material reprocessing, a consistent chemistry regulates the transition from protostellar envelopes to comets over time. Additionally, the correlation between CH_3CN and CH_3OH in comets appears to be weaker than in hot corinos, and it shows a potential dichotomy that might be related to different formation epochs, different formation regions in the disk, or post-formation thermal processing.
Conclusions. A statistical and multidisciplinary approach is essential to establish a robust baseline for characterizing the heterogeneity of planet-forming regions and comets. This helps us to identify differences and caveats that would remain hidden in single-source studies, with the risk of biasing the resulting conclusions. The expansion of these sample sizes will provide the statistical power needed to investigate the origins of our planetary system and other planetary systems.

Key words. astrochemistry – comets: general – planets and satellites: formation – protoplanetary disks – stars: formation – ISM: molecules

1. Introduction

The chemical history of the Solar System is imprinted upon its small bodies. These include comets, which are frozen primitive bodies that provide one of the most pristine fingerprints of the protosolar disk composition during the era of planet formation. The comparison of their composition with that of young solar analogs, that is, low-mass protostellar sources and planet-forming disks from the Class 0/I stages (10^4–10^5 years) to the Class II (10^6 years) (e.g., Ceccarelli et al. 2023), allows us to investigate the extent of the chemical inheritance throughout the star formation process and to identify key clues on the disk-processed material that was incorporated within cometary bodies (Mumma & Charnley 2011; Lippi et al. 2024; Willacy et al. 2025). In particular, it is highly debated whether the chemical complexity observed at the protostellar stage is preserved in time from the early star formation stages up to the formation of planetary bodies in the disks or if the initial protosolar chemical composition was instead reprocessed (i.e., inheritance vs reset scenarios, Ceccarelli et al. 2023). Despite the clear need of testing these two scenarios, systematic comparisons between the chemical composition of protostellar environments, disks, and comets remain rare.

Existing comparative studies are typically limited to only a few prototypical hot corinos and disks and a very small sample of comets, frequently just with the extensively observed Jupiter-family comet 67P/Churyumov-Gerasimenko (hereafter 67P) from the ESA-Rosetta mission (e.g., Drozdovskaya et al. 2019; Bianchi et al. 2019; Yamato et al. 2024; Fadul et al. 2025; Booth et al. 2025). More recently, statistical considerations are becoming central to the field, with Lippi et al. (2024), who compared the abundance ratios of [CH_3OH]/[H_2CO] and [NH_3]/[CH_3OH] across 35 comets and 11 planet-forming systems for the first time, and Willacy et al. (2025), who applied the method of Drozdovskaya et al. (2019) to investigate interstellar complex molecules in 12 comets and the protostar IRAS

⋆ Corresponding author: manuela.lippi@inaf.it

Open Access article, published by EDP Sciences, under the terms of the Creative Commons Attribution License (https://creativecommons.org/licenses/by/4.0), which permits unrestricted use, distribution, and reproduction in any medium, provided the original work is properly cited.
This article is published in open access under the Subscribe to Open model. Subscribe to A&A to support open access publication.

Table 1. Mixing ratios with respect to water of methyl cyanide and methanol, and relative abundance ratios ([CH_3CN]/[CH_3OH]) in comets.

Comet	Dynamical Class	$R_h^{(a)}$ (au)	CH_3CN % wrw	CH_3OH % wrw	[CH_3CN]/[CH_3OH]	Refs
21P/Giacobini-Zinner$^{(b)}$	JF	1.02	0.026 ± 0.003	1.70 ± 0.10	0.0153 ± 0.0020	(1)
46P/Wirtanen$^{(b)}$	JF	1.06	0.017 ± 0.001	3.38 ± 0.03	0.0050 ± 0.0003	(2)
46P/Wirtanen$^{(b)}$	JF	1.10	0.011 ± 0.002	2.70 ± 0.10	0.0041 ± 0.0008	(3)
67P/C.G.$^{(b)}$	JF	1.22	0.017 ± 0.003	1.20 ± 0.10	0.0142 ± 0.0028	(4)
153P/Ikeya–Zhang$^{(b)}$	LP	1.00	0.016 ± 0.004	2.5 ± 0.1	0.0064 ± 0.0016	(5)
C/1995 O1 (Hale-Bopp)$^{(b)}$	LP	1.00	0.020 ± 0.004	2.4 ± 0.1	0.0083 ± 0.0018	(6)
C/2000 WM1 (LINEAR)	DN	1.33	0.014 ± 0.004	1.3 ± 0.2	0.0108 ± 0.0035	(5)
C/2001 A2 (LINEAR)$^{(b)}$	LP	1.16	0.028 ± 0.010	2.8 ± 0.4	0.0100 ± 0.0038	(5)
C/2002 X5 (Kudo-Fujikawa)	LP	0.20	0.016 ± 0.006	2.4 ± 0.2	0.0067 ± 0.0026	(7)
C/2006 P1 (McNaught)	DN	0.26	0.008 ± 0.003	0.6 ± 0.2	0.0133 ± 0.0067	(7)
C/2014 Q2 (Lovejoy)$^{(b)}$	LP	1.30	0.015 ± 0.003	2.4 ± 0.5	0.0063 ± 0.0018	(8)
C/2020 F3 (NEOWISE)$^{(b)}$	LP	0.70	0.011 ± 0.003	2.3 ± 0.1	0.0048 ± 0.0013	(9)
C/2021 A1 (Leonard)	DN	0.80	0.016 ± 0.001	0.88 ± 0.02	0.0182 ± 0.0012	(10)
C/2022 E3 (ZTF)$^{(b)}$	DN	1.18	0.017 ± 0.001	1.76 ± 0.01	0.0097 ± 0.0006	(10)
67P-Summer Hemisphere	JF	3.10	0.006 ± 0.001	0.31 ± 0.06	0.0194 ± 0.0041	(11)
67P-Winter Hemisphere	JF	3.10	0.016 ± 0.003	0.55 ± 0.11	0.0291 ± 0.0062	(11)
67P-Bulk	JF	–	0.0059 ± 0.0034	0.21 ± 0.06	0.0280 ± 0.0180	(12)
3I/ATLAS	ISO	1.37	0.023 ± 0.006	5.1 ± 0.1	0.0045 ± 0.0012	(13)

Notes. $^{(a)}$Heliocentric distance at the time of observations.$^{(b)}$For these comets, the MRs were averaged over different epochs, but at similar heliocentric distances, as reported in the respective references. References: (1) Biver et al. (2021b); (2) Biver et al. (2021a); (3) Cordiner et al. (2023); (4) Biver et al. (2023); (5) Biver et al. (2006); (6) Bockelée-Morvan et al. (2000); (7) Biver et al. (2011); (8) Biver et al. (2015); (9) Biver et al. (2022); (10) Biver et al. (2024a); (11) Le Roy et al. (2015); (12) Rubin et al. (2019); (13) Biver et al. (2026).

16293-2422B. While the former study suggested that cometary methanol, ammonia, and formaldehyde might be inherited from the early stages of Solar System formation, the latter demonstrated that most of the more complex species can deviate from protostellar compositions. This implies that comets preserve a mix of the inherited and the disk-processed material.

We follow the method implemented in Lippi et al. (2024) here to investigate the abundance ratio of methyl cyanide (CH_3CN) relative to methanol (CH_3OH) in a sample of 13 comets, 24 hot corinos of low-mass protostars, and seven protoplanetary disks in different evolutionary stages. In Section 2.1 we first perform a statistical analysis of the cometary database to search for possible correlations and trends in the data. We then expand this statistical analysis to interstellar and circumstellar environments: Section 2.2 focuses on the statistics of hot corinos, while Section 2.3 details the statistics of protoplanetary disks. In Section 3 we discuss the [CH_3CN]/[CH_3OH] abundance ratio and the observed correlation between these two molecular species in different environments. Finally, in Section 3.3, we briefly discuss the caveats that might affect the observed molecular abundances in these different environments, and consequently, their interpretation in the context of planet formation.

2. Methyl cyanide and methanol in comets and star- and planet-forming regions

Methyl cyanide is one of the simplest organic nitriles and one of the most frequently observed species in environments ranging from the earliest evolutionary stages of low-mass star formation to comets (Yang et al. 2021; Belloche et al. 2020; Öberg et al. 2015; Biver et al. 2024b). A strong correlation between CH_3OH and CH_3CN has been observed in hot corinos around young solar analogs (Belloche et al. 2020; Yang et al. 2021; van't Hoff et al. 2024) and in massive clumps in different evolutionary stages (Giannetti et al. 2017). Two main formation mechanisms for methyl cyanide have been proposed: via grain-surface reactions (Garrod 2008; Hasegawa & Herbst 1993; Enrique-Romero & Lamberts 2025), and via gas-phase reactions (Herbst 1985; Klippenstein 1996; Geppert et al. 2007; Garrod et al. 2022; Giani et al. 2023). So far, icy CH_3CN has not been unambiguously detected (Rachid et al. 2022). Giani et al. (2023) discussed that the observed correlation is compatible with the gas-phase formation path and that this might arise because when it is released into the gas phase in the sublimation region, CH_3OH reactions with H_3^+ form CH_3^+ ($CH_3OH + H_3^+ \rightarrow CH_3^+ + H_2 + H_2O$). The CH_3^+ cation is the starting point of the efficient gas-phase formation of CH_3CN via radiative association of CH_3^+ and HCN, forming CH_3CNH^+ ($CH_3^+ + HCN \rightarrow CH_3CNH^+ + h\nu$), followed by electron recombination ($CH_3CNH^+ + e^- \rightarrow CH_3CN + H$). By tracking the evolution of the [CH_3CN]/[CH_3OH] abundance ratio from protostars to comets, we might thus reveal the chemical history of CH_3CN.

2.1. Comets

The mixing ratios[1] (MR) of methyl cyanide are reported in the literature for 13 comets (see Table 1 and references therein). They are mostly retrieved from millimeter spectra because this molecule has only a few weak lines in the infrared, and suitable models for interpreting these lines have yet to be developed. We report the corresponding production rates (molecules/s) in Table A.1 in Appendix A. In addition, we report in Table 1 a few values from in situ measurements of 67P and for the Interstellar

[1] We use the term MR for comets to indicate the relative abundance of a molecule with respect to water in percent.

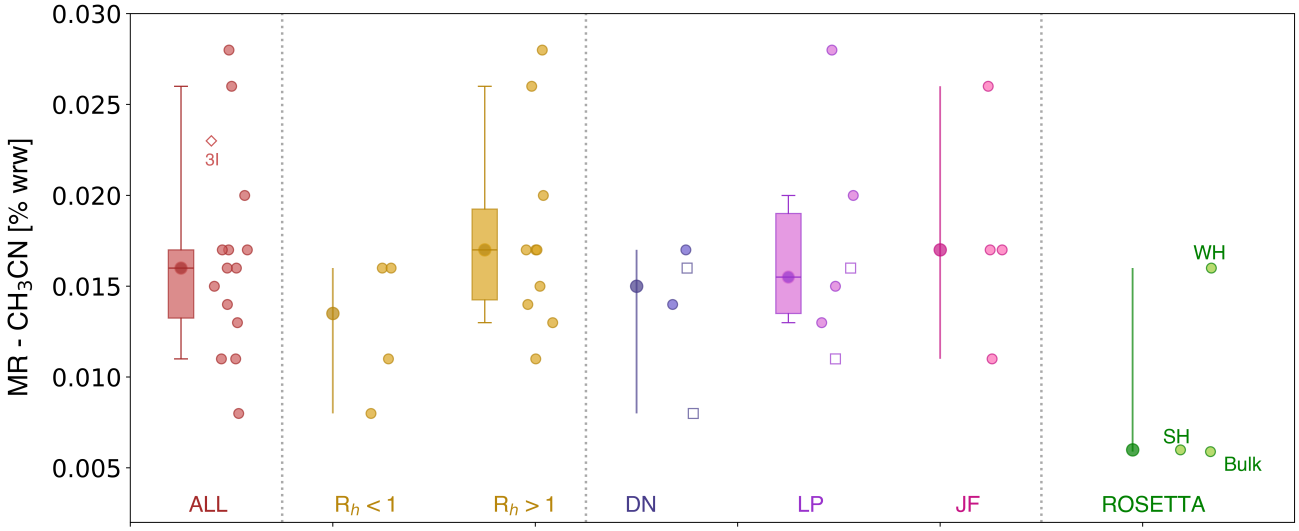


Fig. 1. Box plot statistics for CH_3CN in comets. Starting from the left, we show the overall database, the heliocentric distance dependence (R_h < 1 vs. R_h > 1 au), and different dynamical types (DN, LP, and JF). In green we report the ROSINA-Rosetta measurements for 67P. 3I is shown together with all the Solar System comets as an empty red diamond. For each box plot, the middle line corresponds to the median, the box limits to the 25th and 75th percentiles, and the whiskers to the 5th and 95th percentiles. When we show different dynamical groups, comets observed within 1 au from the Sun are indicated with an empty square. The statistical results are reported in Table A.2.

object (ISO) 3I/ATLAS (hereafter 3I) that was recently observed by Biver et al. (2026). In Table 1 we also report the MRs measured for methanol and the abundance ratios [CH_3CN]/[CH_3OH] that we used for comparisons with star- and planet-forming regions (see Section 3). A comprehensive statistical analysis for methanol comprising a much larger sample of comets can be found in Lippi et al. (2024).

The overall MR statistical analysis for methyl cyanide is shown in Figure 1 and reported in Table A.2 in Appendix A. Following Lippi et al. (2024), we divided the data into subsamples and investigated whether the MRs of CH_3CN varied with the heliocentric distances (R_h) or the dynamical class, i.e., dynamically new (DN), long period (LP), and Jupiter family (JF) comets. The former might reflect temperature-activated chemical processes in the coma, while the latter might indicate signatures of chemical evolution after formation.

The MRs of CH_3CN with respect to water in comets range from 0.008% to 0.028%, with a median value and dispersion of 0.016% and 0.005%, respectively. The values measured in comets observed at heliocentric distances shorter than 1 au seem to decrease slightly compared to those measured at larger distances (see Fig. 1), as was already observed for CH_3OH (see Lippi et al. 2024). However, as for methanol, these differences are not statistically significant. We identified no significant differences between different dynamical classes. On the other hand, the sizes of the subsamples are too small to reach a firm conclusion. Based on the ROSINA-Rosetta measurements reported in Le Roy et al. (2015) and on the deduced bulk abundances from Rubin et al. (2019), methyl cyanide in the winter hemisphere (WH) of 67P is consistent with the cometary average. Conversely, the summer hemisphere (SH) and bulk compositions (Bulk) seem to show lower MRs than the median value retrieved from ground-based measurements. These differences might depend in part on the large heliocentric distance at the time of observations (≈3 au) and on potential uncertainties within the model-dependent retrievals that were used to calculate the bulk abundances (Rubin et al. 2019). The CH_3CN and CH_3OH MRs measured for the interstellar object 3I by Biver et al. (2026) are also in line with Solar System comets, despite the clearly different nature of this object (e.g., Cordiner et al. 2026; Opitom et al. 2026). Finally, we note that spectrally integrated emission maps of CH_3CN and CH_3OH in the coma of 46P/Wirtanen (Cordiner et al. 2023) and 12P/Pons-Brooks (Cordiner et al., in prep.), obtained with the Atacama Large Millimeter Array (ALMA), both exhibit a spatial distribution consistent with a parent species[2]. While a larger statistical sample is required to confirm these trends, these two examples strongly indicate that for the majority of comets, the observed [CH_3CN]/[CH_3OH] ratio can be considered representative of the nucleus composition.

2.2. Protostellar sources: The PEACHES, CALYPSO, and PILS surveys

In the hot corino region around low-mass protostellar objects, the temperature is >100 K, and the icy grain mantles are therefore released into the gas phase, and the molecular abundances estimated from molecular emission lines are thought to reflect the ice composition. In Table 2 we report the column densities of CH_3CN and CH_3OH and the [CH_3CN]/[CH_3OH] abundance ratios estimated for a total of 22 protostellar sources observed by the PEACHES (Yang et al. 2021), CALYPSO (Belloche et al. 2020), and PILS (Jørgensen et al. 2016) surveys.

The PEACHES survey targets a large sample of Class 0 and I protostellar sources, located at distances spanning from 234 pc to 331 pc in the active and nearby Perseus star-forming region (Ortiz-León et al. 2018a; Zucker et al. 2019). The observations were taken with ALMA and cover several spectral windows in Band 6 (1.3 mm) at an angular resolution of about 0.″5. The detected CH_3CN and CH_3OH emission lines were fitted assuming that the lines originate in the same region and that the

[2] Parent (or primary) species refer to molecules that sublimate directly from the cometary nucleus, making them representative of the bulk composition, while daughter (or secondary) molecules are products of photodissociation and/or gas-phase reactions of parent molecules in the coma.

Table 2. Column densities and abundance ratios of CH_3CN and CH_3OH in low-mass protostars from the PEACHES, CALYPSO, and PILS surveys.

Protostar	CH_3CN (10^{14} cm^{-2})	CH_3OH (10^{16} cm^{-2})	[CH_3CN]/[CH_3OH]
ALMA PEACHES[(a)]			
L1448N-A	$0.85^{+0.43}_{-0.35}$	$0.53^{+0.19}_{-0.28}$	$0.016^{+0.012}_{-0.009}$
L1448-3A	$1.7^{+0.8}_{-0.7}$	$0.84^{+0.45}_{-0.53}$	$0.020^{+0.016}_{-0.014}$
L1448-C	15^{+7}_{-6}	$8.9^{+3.2}_{-4.4}$	$0.017^{+0.011}_{-0.009}$
L1448-2A	$1.8^{+0.9}_{-0.8}$	$2.0^{+1.1}_{-1.2}$	$0.009^{+0.007}_{-0.006}$
L1448-2B	$1.6^{+0.7}_{-0.7}$	$1.6^{+0.7}_{-1.0}$	$0.010^{+0.008}_{-0.006}$
L1455-4	<0.7	$1.3^{+0.8}_{-0.8}$	<0.0053
SVS-13A	59^{+18}_{-13}	81^{+50}_{-31}	$0.007^{+0.004}_{-0.005}$
IRAS-4A2	29^{+11}_{-10}	20^{+10}_{-1}	$0.014^{+0.006}_{-0.009}$
IRAS-4B1	$7.3^{+3.2}_{-2.5}$	$5.0^{+3.3}_{-3.2}$	$0.015^{+0.011}_{-0.011}$
IRAS-2A1	65^{+21}_{-13}	110^{+10}_{-50}	$0.006^{+0.003}_{-0.001}$
IRAS-1A	$5.0^{+2.5}_{-2.1}$	$5.3^{+2.2}_{-2.9}$	$0.009^{+0.007}_{-0.006}$
IRAS-1B	$0.69^{+0.35}_{-0.29}$	$0.63^{+0.30}_{-0.35}$	$0.011^{+0.008}_{-0.007}$
IRAS-7-SM1	$2.3^{+0.1}_{-1.0}$	$2.3^{+1.0}_{-0.1}$	$0.010^{+0.001}_{-0.006}$
B1-b S	$3.2^{+1.6}_{-1.4}$	$1.5^{+0.1}_{-0.9}$	$0.021^{+0.017}_{-0.009}$
B1-c	11^{+5}_{-4}	$9.0^{+6.3}_{-5.9}$	$0.012^{+0.010}_{-0.010}$
IRAS 03282+3035	$1.8^{+0.8}_{-0.8}$	$0.99^{+0.47}_{-0.60}$	$0.018^{+0.014}_{-0.012}$
HH 211 MMS	$0.62^{+0.31}_{-0.26}$	$0.89^{+0.38}_{-0.54}$	$0.007^{+0.005}_{-0.004}$
IC 348 MMS	$1.4^{+0.7}_{-0.6}$	$0.91^{+0.53}_{-0.56}$	$0.015^{+0.012}_{-0.011}$
IRAM PdBI CALYPSO[(b)]			
L1448-2A	2.2	0.5	0.0440
L1448-C	25	8	0.0313
*IRAS-2A1	250	180	≤0.014
SVS-13A	400	200	0.020
*IRAS-4A2	110	60	≤0.018
*IRAS-4B1	25	15	≤0.017
*SerpM-S68N	8	3	≤0.027
*SerpS-MM18a	130	22	≥0.059
SerpS-MM18b	4.7	1.7	0.028
*L1157	46	13	≤0.035
ALMA PILS[(c)]			
IRAS-16293A	800 ± 100	1300 ± 400	0.006 ± 0.002
IRAS-16293B	400 ± 100	1000 ± 200	0.004 ± 0.001

Notes. The asterisk indicates sources for which the estimated temperatures are different by more than 25% for the two species. The estimated abundance ratios are therefore lower or upper limits as explained in the text; the CALYPSO survey does not report error bars. [(a)]The data are from Yang et al. (2021). For this, the temperature was assumed (T_{ex} = 100, 150, 200, 250, and 300 K), and the corresponding mean column density value and uncertainty over the temperature range were inferred assuming LTE optically thin emission. The uncertainties on the [CH_3CN]/[CH_3OH] ratio were calculated considering error propagation rules for the upper and lower bounds separately. [(b)]The data are from Belloche et al. (2020). The column density and temperature were estimated for each species from a multi-line fit, assuming LTE. [(c)]The data are from Jørgensen et al. (2016, 2018); Calcutt et al. (2018); Manigand et al. (2020).

emission is optically thin and in local thermodynamic equilibrium (LTE). Yang et al. (2021) fitted the observed lines with five temperatures values (T_{ex} = 100, 150, 200, 250, and 300 K) and took the column density as the mean derived value and the uncertainty as the range of the fitted column densities.

The CALYPSO survey also targets a sample of solar-type protostars, including Class 0 and Class I sources associated with hot corino emissions, located in the nearby star-forming regions of Perseus (some in common with the PEACHES survey), Serpens Main and South, and Cepheus (at distances of 293 pc, 436 pc, 350 pc, 352 pc, respectively, see Ortiz-León et al. 2018a,b; Zucker et al. 2019). The observations were taken with the Plateau de Bure Interferometer (PdBI) of the Institute de Radioastronomie Millimétrique (IRAM) with three spectral setups (at 1.30, 1.37, and 3.19 mm) with an angular resolution of 0.″5−1.″. The detected CH_3CN and CH_3OH emission lines were fitted assuming LTE with the Weeds package (Maret et al. 2011) of the CLASS software, which takes the angular resolution of the telescope and the opacity of the transitions into account. The estimated excitation temperatures of methanol and methyl cyanide in the CALYPSO survey are between 100 and 200 K (Belloche et al. 2020). For some sources the estimated excitation temperature of methanol is higher than that of methyl cyanide ($T_{ex}(CH_3OH) > T_{ex}(CH_3CN)$). Since the temperature in a hot corino decreases exponentially with the distance from the protostar (e.g., Frediani et al. 2025), the estimated excitation temperature reveals the specific region in which each molecule is in the gas phase. Therefore, $T_{ex}(CH_3OH) > T_{ex}(CH_3CN)$ suggests that the CH_3OH emission originates in a warmer, and thus, more compact, region than CH_3CN. This implies that for these sources, methanol remains partially frozen out in the outer region in which methyl cyanide is observed, thereby skewing the [CH_3CN/CH_3OH] abundance ratio toward higher values. In these cases, if the difference in temperature exceeds 25%, we assumed that the abundance ratio [CH_3CN]/[CH_3OH] is an upper limit, even though methanol and methyl cyanide are reported as detections. An exception is provided by SerpS-MM18a, for which the CH_3OH excitation temperature is lower than for CH_3CN, implying a puzzling more extended region for methanol. We took the resulting abundance ratio [CH_3CN]/[CH_3OH] as a lower limit.

For completeness, we added the two prototypical Class 0 hot corinos IRAS 16293-2422A and IRAS 16293-2422B surveyed by the ALMA program PILS (Jørgensen et al. 2016, 2018; Calcutt et al. 2018; Manigand et al. 2020) since they are often used as a reference for comparisons with comets (e.g., Drozdovskaya et al. 2019; Willacy et al. 2025). Finally, we considered recent estimates of CH_3CN abundances in four hot corinos as retrieved by Nazari et al. (2024) from the fit of ice absorption features observed using the James Webb Space Telescope (JWST). The authors reported surprisingly high [CH_3CN]/[CH_3OH] abundance ratios (≈0.2–0.3), although these values were noted as tentative detections. Since an unambiguous identification of solid methyl cyanide from these spectra is challenging (Rachid et al. 2022), we assumed these results as upper limits (see Figure 2).

2.3. Planet-forming disks

We summarize the column densities of methyl cyanide and methanol in seven disks from the Class 0 to the Class II stages in Table 3. For each species, we report the excitation temperature and column density estimated from multi-line rotational diagram analysis, assuming LTE and optically thin emission. When only one or a few lines are observed, the temperature is assumed and reported in parentheses. When the estimated excitation temperature for CH_3CN is lower than methanol sublimation temperature (i.e., T < 80 K, Ferrero et al. 2020; Kakkar et al. 2025), the

Table 3. Column densities of CH_3CN and CH_3OH in outbursting and quiescent planet-forming disks.

Protostar	CH_3CN (cm^{-2})	T_{CH_3CN} (K)	CH_3OH (cm^{-2})	T_{CH_3OH} (K)	$[CH_3CN]/[CH_3OH]$	Refs
Class 0 – Outbursting						
V883 Ori[(a)]	$2.45^{+0.26}_{-0.25}(10^{15})$	120	$3.6^{+0.4}_{-0.4}(10^{18})$	120	$0.0007^{+0.0001}_{-0.0001}$	(1)
V883 Ori[(b)]	$3^{+0.2}_{-0.2}(10^{16})$	120	$4^{+0.8}_{-0.8}(10^{19})$	120	$0.0008^{+0.0002}_{-0.0002}$	(2)
V883 Ori[(c)]	$4^{+2}_{-2}(10^{14})$	252	$4^{+15}_{-3}(10^{18})$	100	>0.0001	(3)
Class I and II – Outbursting						
L1551 IRS5[(d)]	$1.6^{+0.1}_{-0.1}(10^{17})$	178	$5.5^{+0.3}_{-0.3}(10^{19})$	178	$0.0029^{+0.002}_{-0.002}$	(4)
V1057 Cyg	$1.0 \pm 0.20\ (10^{13})$	110	$3.2 \pm 0.64\ (10^{15})$	180	<0.003	(5)
Class II						
TW Hya	$1.5^{+0.2}_{-0.2}(10^{12})$	33	$3.5^{+1.3}_{-0.4}(10^{12})$	36	$0.42\ ^{+0.075}_{-0.169}$	(6,7,8)
HD 100546	$<2.0(10^{13})$	[152]	$1.4^{+0.3}_{-0.4}(10^{14})$	152	< 0.142	(9,10)
Oph IRS48	$<3.5(10^{13})$	[100]	$2.2^{+0.5}_{-0.5}(10^{14})$	[100]	<0.159	(11)
HD 100453[(e)]	$4.7^{+2.0}_{-1.1}(10^{13})$	50	$5.2^{+0.35}_{-0.23}(10^{16})$	190	≤0.0009	(12)

Notes. The temperature values in parentheses are assumed. [(a)]The column densities were derived assuming LTE at $T_{ex} \sim 120$ K ($T_{ex} \sim 92 \pm 4$ K from $^{13}CH_3OH$). N(CH_3OH) was inferred from its rarer isotopolog $CH_3^{18}OH$, assuming an isotopic ratio $^{18}O/^{16}O$=557. [(b)]The column densities were derived from an iterative LTE line-fitting procedure using only isolated optically thin lines (T_{ex} = 120 K) and using their rarer isotopologs, either $CH_3^{18}OH$ (for CH_3OH), or ^{13}C (for CH_3CN). [(c)]The column densities were derived assuming LTE for each species separately. N(CH_3OH) was inferred from its rarer isotopolog $CH_3^{18}OH$, assuming an isotopic ratio $^{18}O/^{16}O$ = 557. [(d)]The column densities in outbursting protostellar sources were derived from LTE fitting by Cruz-Sáenz de Miera et al. (2025). The column density were determined for all species for the same T_{ex}, line center and width, and source size. [(e)]The column densities were derived assuming LTE, and N(CH_3OH) was inferred from its rarer isotopolog, $^{13}CH_3OH$, assuming an isotopic ratio $^{12}C/^{13}C$ = 69. References: (1) Lee et al. (2019); (2) Jeong et al. (2025); (3) Fadul et al. (2025); (4) Cruz-Sáenz de Miera et al. (2025); (5) Calahan et al. (2024) (6) Loomis et al. (2018); (7) Walsh et al. (2016); (8) Ilee et al. (2026); (9) Booth et al. (2024a); (10) Evans et al. (2025); (11) Booth et al. (2024b); (12) Booth et al. (2025).

species do not originate in the inner disk region, where sublimation dominates and the icy mantles are released in the gas phase. Instead, low temperatures indicate release through nonthermal processes or molecular formation through gas-phase reactions. Therefore, the derived column densities cannot be used as a probe of the ice composition (e.g., for the disk TW Hya).

In HD 100546 and Oph IRS48, only methanol is detected, and we were only able to place an upper limit on the CH_3CN column density, and hence, on the $[CH_3CN]/[CH_3OH]$ abundance ratio. For HD 100453 and the outbursting disk V1057 Cyg, the excitation temperature of methanol is remarkably higher than that of methyl cyanide, possibly because the molecules trace different regions in these disks, with CH_3OH probing thermal sublimation in the inner region, and CH_3CN that might form through cooler gas-phase processes at larger disk radii. Following the same procedure as adopted for hot corinos, we took the abundance ratios $[CH_3CN]/[CH_3OH]$as an upper limit when the temperatures of the two species differed by more than 25%.

For V883 Ori, we have multiple measurement of methanol and methyl cyanide column densities (Lee et al. 2019; Jeong et al. 2025; Fadul et al. 2025). While Lee et al. (2019) and Jeong et al. (2025) fitted the molecular line emissions assuming the same temperature for the two species (T = 120 K), Fadul et al. (2025) estimated a temperature for methyl cyanide (≈252 K) that is much higher than that of methanol (≈100 K). This implies a more extended emitting region for methanol, meaning that methyl cyanide is partially still frozen in the region in which we measure methanol. Thus, the $[CH_3CN]/[CH_3OH]$ abundance ratio is biased toward lower values, and we took the resulting abundance ratio $[CH_3CN]/[CH_3OH]$ as a lower limit, although both species are detected (see Table 3).

Recently, Booth et al. (2026) reported observations of CH_3OH and CH_3CN in other Herbig systems (i.e., F- and A-type stars). We omit these disks in Table 3 and Figure 2 since only one line per species was observed and the temperature could not be determined. Furthermore, at least one of the chemical species in these systems is reported as an upper limit.

3. Results and discussion

3.1. A similar chemistry in hot corinos and comets as opposed to the high heterogeneity of disks

The $[CH_3CN]/[CH_3OH]$ abundance ratios in different astrochemical environments are shown in Figure 2. Overall, the hot corino surveys cover a range of ratios from ≈0.004 to 0.044. The values retrieved for the PEACHES survey (median of 0.012 ± 0.005) and the PILS survey (≈0.005) agree with those measured in the cometary sample (median of 0.009 ± 0.004). The CALYPSO survey shows the highest median value (0.029 ± 0.008) compared to the PEACHES and PILS surveys, and to comets. However, these differences stay inside an order of magnitude and are consistent at the 2σ level (see Table B.1 and Figure B.1 in Appendix B). The lower $[CH_3CN]/[CH_3OH]$ ratios estimated for IRAS 16293 A and IRAS 16293 B are likely due to the PILS survey's use of isotopologs. By observing these rarer species, PILS accounts for opacity effects that are stronger for abundant species such as methanol (see Section 3.3). Consequently, the methanol abundance in the CALYPSO and PEACHES surveys might be underestimated, leading to their higher reported $[CH_3CN]/[CH_3OH]$. Dynamically new comets are the most consistent with hot corinos, displaying

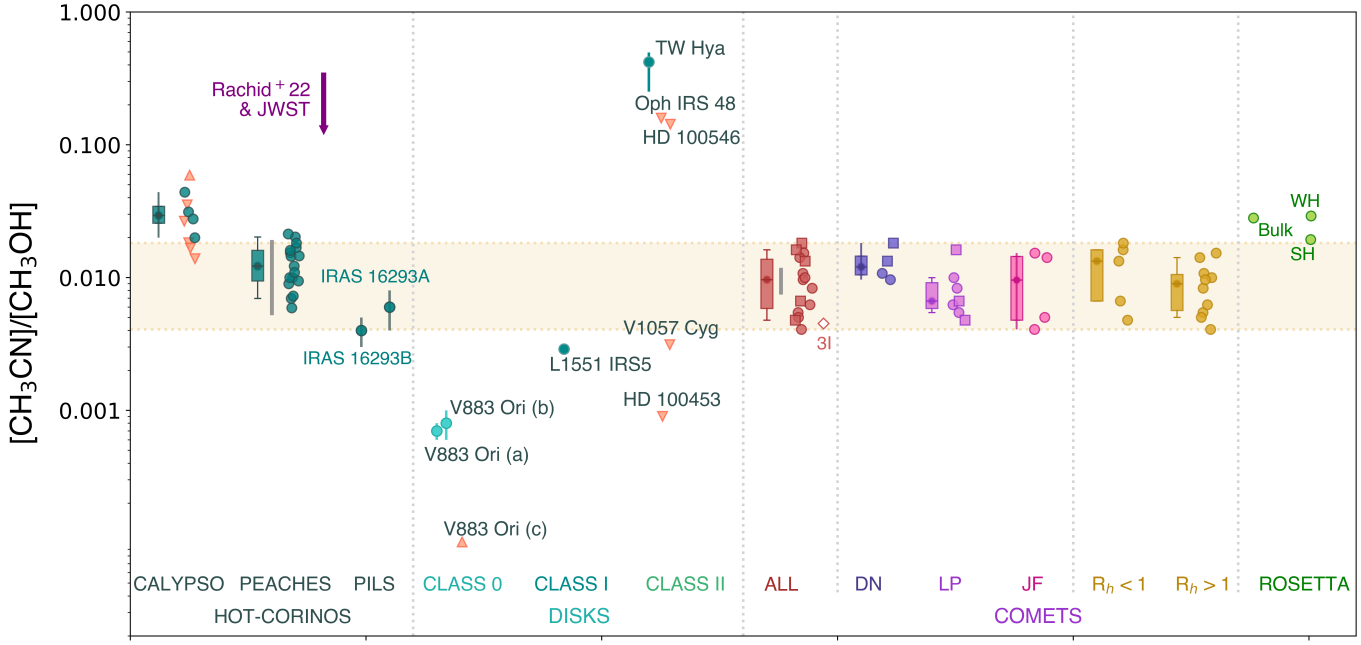


Fig. 2. Box plot statistic for $[CH_3CN]/[CH_3OH]$ ratios in comets and comparison with star- and planet-forming regions. Starting from the left, we show the ratios measured in the CALYPSO, PEACHES, and PILS surveys, Class 0, Class I, and Class II disks, and comets. For hot corinos, we also indicate in pink the upper limits predicted by Rachid et al. (2022) and measured with the JWST (Nazari et al. 2024). The abundance ratios estimated in hot corinos and disks are shown by using a different color/symbol coding: when the difference in temperature does not exceed 25%, we use filled circles, and otherwise, we use red upward/downward triangles indicating lower/upper limits of $[CH_3CN]/[CH_3OH]$. The comets are shown all together, sorted by different dynamical families (DN, LP and JF), and different heliocentric distances ($R_h < 1$ vs. $R_h \geq 1$ au). When all together and grouped by dynamical families, squares and circles indicate comets observed at $R_h < 1$ au and $R_h \geq 1$ au, respectively. The last points refer to mass spectrometer measurements of 67P during the ESA-Rosetta mission. The horizontal filled light orange bar includes all the cometary values measured from ground-based facilities. For the PEACHES survey and for comets, the vertical gray line between the box plot and the data points represents the average uncertainty of individual measurements.

$[CH_3CN]/[CH_3OH]$ abundance ratios higher than the cometary average. This suggests that dynamically new comets have either undergone less thermal processing than long-period and Jupiter-family comets, thus preserving a more pristine chemical signature, or that they originated in a different region or epoch of the protoplanetary disk. Finally, we note that the $[CH_3CN]/[CH_3OH]$ ratio measured in situ for 67P (median of 0.028 ± 0.004) is also statistically comparable with hot corino values and only slightly higher than ground-based measurements for other comets. The same applies to the interstellar object 3I, which exhibits a lower but comparable $[CH_3CN]/[CH_3OH]$ ratio of 0.0045 ± 0.0012. For the PEACHES and cometary samples, the datasets allowed us to compare the average uncertainty of individual measurements against the overall statistical dispersion (see Figure 2). Interestingly, for hot corinos in the PEACHES survey, the individual measurement uncertainties are larger than the dispersion of the median value. In contrast, the data dispersion for comets is larger than the individual error bars. This suggests that while the PEACHES sample is statistically consistent, the comet data might be affected by additional sources of variance (see Section 3.3).

In planet-forming regions, the Class I source L1551 IRS5 shows a $[CH_3CN]/[CH_3OH]$ abundance ratio that is slightly lower but still similar to that of hot corinos and comets (≈0.003). The upper limits retrieved for HD 100546 and Oph IRS48 agree with the hot corino values, whereas the upper limit for HD 100546 is inconsistent with this range. For the latter source, however, the very different excitation temperatures retrieved for CH_3CN (50 K) and CH_3OH (228 K) suggest that the emissions arise from very different regions in the disk. We also note that HD 100546, Oph IRS48, and HD 100543 are Herbig systems (F- and A-type stars) and are therefore less representative of a young solar-type star. The Class 0 V883 Ori and the Class I–II TW Hya and V1057 Cyg disks show contrasting results, with abundance ratios ranging from the very low value of ≈0.0007 for V883 Ori to ≈0.43 for TW Hya. For these sources, the observed differences are puzzling, and it remains a complex challenge to interpret these results within the framework of inheritance versus reset scenarios.

To explain the high abundance ratio measured in TW Hya, we note that the estimated excitation temperature is ≈35 K, that is, much lower than the methanol and methyl cyanide sublimation temperature (T > 80 K, e.g., Kakkar et al. 2025). Since TW Hya is a cold disk, nonthermal desorption, possibly followed by gas-phase formation of CH_3CN, controls the molecular abundances in the outer disk, where a carbon-rich chemistry has been revealed (Calahan et al. 2023). Hence, the measured $[CH_3CN]/[CH_3OH]$ abundance ratio for this source is not representative of the ice composition.

V883 Ori and V1057 Cyg are instead young stellar objects recently undergoing luminosity outburst, estimated to have persisted for decades (Carvalho et al. 2025; Kopatskaia 1984, respectively). It is possible that in these sources, the $[CH_3CN]/[CH_3OH]$ ratio evolves through time. Specifically, an outburst suddenly increases the temperature in the colder outer regions of the disk, triggering the heavy sublimation of methanol-rich ice; this results in the lower observed $[CH_3CN]/[CH_3OH]$ ratio of 0.0007. We expect, however, that over timescales longer than 10^3 years, the gas-phase destruction of the newly released CH_3OH will act as a precursor for CH_3CN

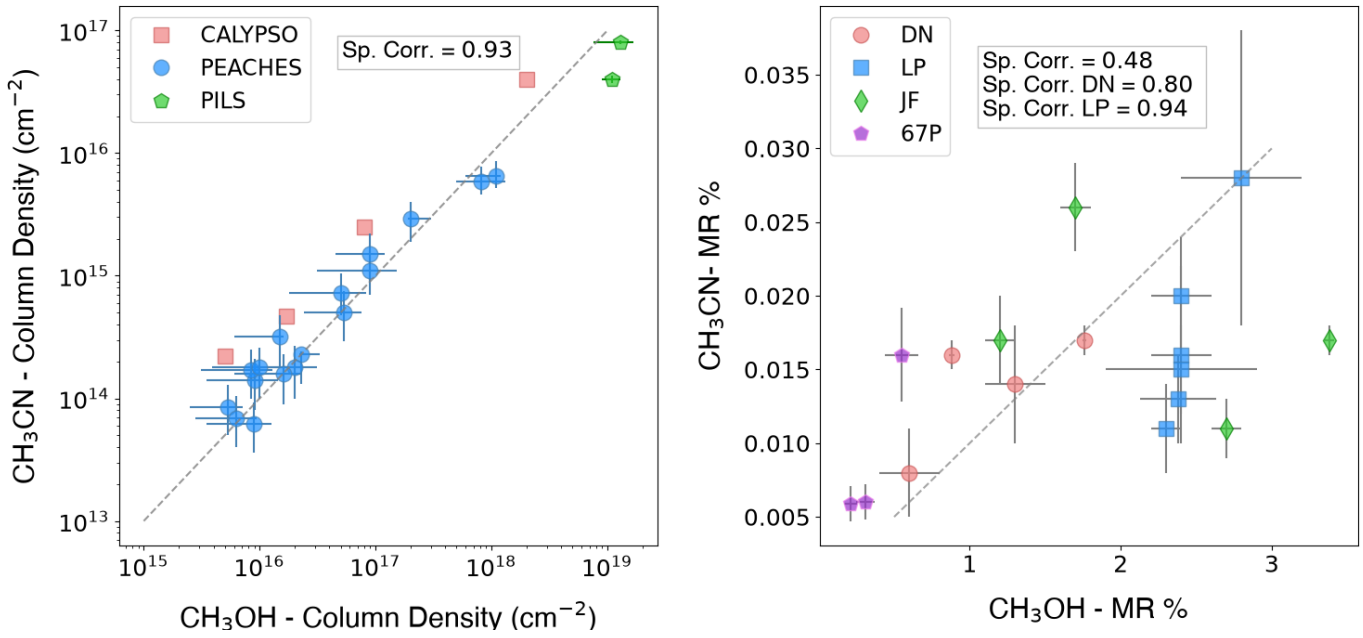


Fig. 3. Correlation plots for CH_3CN and CH_3OH in hot corinos (left) and comets (right). The dotted gray line in the two plots is a reference line indicating the (100:1) ratio.

production, causing the [CH_3CN]/[CH_3OH] ratio to increase to the values typically observed in hot corinos, that is, 1% (Giani et al. 2023). Interestingly, this is what we observe in the case of L1551, which has been in outburst for a longer time ($\approx 10^3$ years, see Beichman & Harris 1981) and shows a [CH_3CN]/[CH_3OH] abundance ratio that is closer to the ratio of hot corinos. The variations in time of methanol and methyl cyanide column densities are also predicted by chemical models, and the low value observed in V883 Ori agrees well with the formation of these species on cold grains before the protostellar heating phase (Garrod et al. 2022).

Alternatively, the low [CH_3CN]/[CH_3OH] abundance ratio in V883 Ori might arise because its disk is embedded, and thus, is shielded from UV radiation. The CH_3CN abundance can be enhanced by the UV flux in the disk atmosphere and the cosmic-ray ionization rate in the UV-shielded midplane due to ion-driven gas-phase synthesis (Giani et al. 2023). Because the disk is embedded, the production of CH_3^+ (a precursor to CH_3CN) is suppressed, and consequently, the [CH_3CN]/[CH_3OH] ratio is lowered. A strong UV illumination might explain the high [CH_3CN]/[CH_3OH] abundance ratio found in the exposed atmosphere of the Class II TW Hya disk.

In either cases, the final agreement between hot corinos and comets suggests that even if significant chemical reprocessing occurs during the Class 0 to Class II disk stages, the chemistry eventually drives the [CH_3CN]/[CH_3OH] ratio back to the $\approx$1% value before the material is incorporated in comets.

3.2. The correlation between methyl cyanide and methanol

We further explored the correlation between methyl cyanide and methanol in hot corinos and comets, as shown in Figure 3, by calculating the Spearman rank-order correlation coefficient (SP) for each sample.

In hot corinos, the very high correlation between these two molecules (SP $\approx$ 0.9) was already reported in Yang et al. (2021) and Belloche et al. (2020). This result indicates a strong chemical relation between CH_3CN and CH_3OH, which might be governed either by the co-formation of the two molecules on grain surfaces or via gas-phase pathways, where methanol serves as a chemical grandparent of methyl cyanide (Giani et al. 2023).

On the other hand, the correlation coefficient SP $\approx$ 0.5 observed in the cometary sample, while still indicating a positive correlation, shows a much more moderate trend compared to that observed in hot corinos. This discrepancy might simply reflect the different scales in the data: while hot corino column densities encompass several orders of magnitude, cometary MRs span a very narrow range. This amplifies the observing uncertainties and variability of the relative CH_3CN and CH_3OH abundances, and thus, it masks the underlying correlation coefficient.

We also note several key differences between comets and hot corinos. The strong correlation observed between CH_3OH and CH_3CN in hot corinos is unlikely to originate in such a scaling effect, since it was observed in more than one sample, and where other molecules show no such correlation with either species. This confirms that the correlation is a real effect, which Giani et al. (2023) explained as due to a chemical link between these two molecules. Specifically, in hot corinos, methanol, which is formed on the grain surfaces, thermally sublimates into the gas phase, where it is destroyed by molecular cations. As briefly described in the beginning of Section 2, one of the important products of the methanol destruction in the gas phase is a precursor of CH_3CN, and astrochemical modeling shows that this is indeed the cause of the correlation. Thus, the CH_3OH-CH_3CN correlation in hot corinos is chemical in origin. On the other hand, cometary abundances reflect material accreted by the nucleus in the protoplanetary disk that sublimates in the coma. Because sublimation is affected by nucleus heterogeneity, varying heliocentric distances, and sparse temporal coverage, the resulting MRs exhibit a larger scatter, which partially disrupts the tight correlation observed in hot corinos.

A closer inspection of the data suggests a potential dichotomy between long-period and dynamically new comets. These two subgroups show higher correlation coefficients (>0.7) when taken separately, with long-period comets also displaying an apparent steeper trend. A possible explanation is that

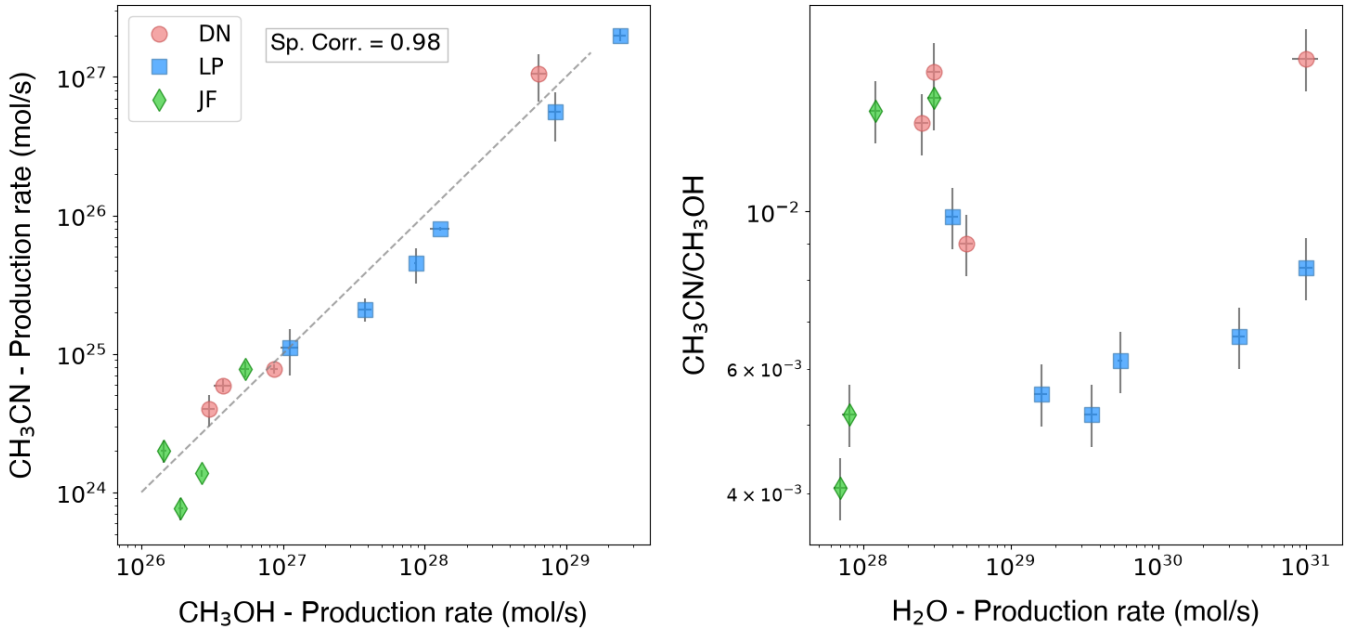


Fig. 4. Left: correlation plot for the production rates of CH_3CN and CH_3OH in comets. The dotted gray line is a reference line indicating the (100:1) ratio. Right: dependence of the [CH_3CN/CH_3OH] ratio on the water production rate.

long-period comets may have undergone thermal reprocessing after incorporation of the material in their nuclei, driven by evolutionary mechanisms such as multiple perihelion passages. Nevertheless, given the similar sublimation temperatures and binding energy distributions of CH_3CN and CH_3OH (see Figure C.1), these processes probably do not account completely for the observed differences. This is strengthened by the fact that the Jupiter-family comets within our sample exhibit a more random scatter in the plot despite having undergone the most extensive thermal processing due to their short periods. Furthermore, chemical processing in the coma can be ruled out, as the comets were observed at comparable heliocentric distances and show no statistically significant variations in MRs closer to the Sun. Consequently, this dichotomy might represent a pristine signature of different accretion times and/or distinct formation regions within the protoplanetary disk before the comets are scattered into their respective reservoirs (Gomes et al. 2005; Brasser & Morbidelli 2013).

We further investigated whether water outgassing might have affected the relative mixing ratios by extending our analysis to production rates (molecules/s) instead of MRs, as shown in the left panel of Figure 4 (the production rates for the different comets are reported in Table A.1). While using production rates improves the CH_3OH–CH_3CN correlation, this trend is most likely scale-driven, since the production rates span several orders of magnitude (10^{27}–10^{29} molecules/s^{-1}), whereas the MRs vary across a much narrower range (0.1–3.5 %). Moreover, since the overall activity of the comet is expected to simultaneously increase the outgassing of all volatile species, this might artificially introduce a strong positive correlation that does not necessarily reflect a shared chemical origin. We thus analyzed the [CH_3CN/CH_3OH] ratio against the H_2O production rate. We note that for our sample, the water production rate is systematically higher in long-period comets, while their [CH_3CN]/[CH_3OH] ratio is systematically lower. While this trend might reflect a possible chemical class with different origins and histories, it might also indicate that water production enhances the release of methanol more than that of methyl cyanide, ultimately lowering the [CH_3CN/CH_3OH] ratio. To confirm these trends, future work should incorporate larger comet sample sizes and emphasize spatial investigations of the coma.

3.3. Observational biases and caveats: Why large samples matter

While our sample provides a robust representation of the target populations, the precision of the derived column densities in planet-forming regions and mixing ratios in comets is still affected by many systematic uncertainties. It is important to note that the emergence of these specific caveats is a direct result of our robust statistics approach. This comprehensive overview not only aids in identifying inconsistencies, but also provides the necessary framework to investigate, at least in part, the underlying drivers of these uncertainties.

One of the primary challenges in retrieving molecular abundances in comets lies in the spatial and environmental variability of the coma as the comet moves through the Solar System. As demonstrated in Lippi et al. (2024), the MRs of some volatile species often exhibit strong dependences and variations based on the heliocentric distance of the comet and on the differential sublimation due to the different volatility of the observed species. Many detected molecules, such as H_2CO, are not only released directly from the nucleus, but also produced by photodissociation of larger species in the coma. Recently, chemical reactions in the coma were invoked to explain the distribution and abundances observed for some molecules (e.g., cyanoacetylene and formamide, see Cordiner & Charnley 2021). The determination of the original cometary composition is further complicated by the inherent diversity within cometary populations, which might stem from their distinct dynamical histories. Abundance retrievals depend on the the rotational excitation in the inner coma, which is governed by collisions with electrons and H_2O molecules (see for example Bockelée-Morvan et al. 2004). However, the exact collisional cross-sections for CH_3OH–H_2O and CH_3CN–H_2O have not yet been determined. The uncertainties on the assumed photodissociation rates can likewise bias the final

results. The MRs are calculated with respect to water, which can be highly variable compared to other molecular species. Our analysis indeed shows that long-period comets are characterized by high water production rates coupled with lower [CH_3CN]/[CH_3OH] abundance ratios, suggesting either a distinct chemical composition or differential molecular release in the coma for this dynamical class. Although water is historically the standard reference as the most abundant cometary species, alternative baselines might be more robust. For example, Bonev et al. (2021) suggested the use of species such as C_2H_6, which are still easily measured in the coma but are less susceptible to variability and coma effects (e.g., extended sources). This approach is currently under investigation by the cometary community and promises to provide new insights into cometary composition in the future. Finally, there is often a noticeable calibration gap between in situ mass and ground-based spectroscopy, since these different techniques probe different scales of the coma and rely on different physical assumptions, making it difficult to create a unified dataset. While current datasets provide a foundational view, they also highlight the need to further increase the sample and resolve the origins of the observed chemical variations.

Also for star- and planet-forming regions, several physical and observational factors can lead to significant misinterpretations of actual column densities. A major problem is dust opacity, which can physically hide the most chemically rich regions of a protostellar source. In many cases, the dust is so thick that molecular spectra must be extracted from a position offset from the continuum peak (see for example the PILS survey, Jørgensen et al. 2016). This spatial shift does not affect all molecules equally; different species can be obscured or revealed to varying degrees, depending on their distribution relative to the dust. Consequently, the derived abundance ratios of different species can be skewed because the sampled area provided by the offset might not be representative of the total chemical inventory of the source. The size of the emitting region introduces further uncertainty, particularly when observations lack the angular resolution to distinguish between different spatial zones. Molecules with higher binding energies only tend to evaporate from dust grains in the innermost hottest regions, while others can exist in more extended cooler envelopes. When a telescope cannot resolve these distinct regions, the resulting data averages the emission over a single area. This means that the calculated abundance ratios are often just lower or upper limits and fail to account for the true spatial distributions. Last, species such as methanol and methyl cyanide are often so abundant in hot corinos and inner disks that their spectral lines become optically thick. In particular, because of its high abundance, CH_3OH is more likely to be more optically thick at a higher gas column density, resulting in an underestimation of its column density. This translate into higher [CH_3CN]/[CH_3OH] ratios. Without detecting rarer isotopologs (e.g., $^{13}CH_3OH$ or $CH_3{}^{18}OH$ to serve as a opacity probe), the estimated column densities for these primary species are frequently recorded as lower limits, making it difficult to accurately compare them against less abundant molecules.

For protoplanetary disks, further sources of uncertainties in retrieving molecular abundances are caused by the complex vertical and radial structure of the disk (e.g., cavities and rings). Moreover, the disk is exposed to UV and X-ray radiation fields from the central star, which might drive gas-phase formation of methyl cyanide (Giani et al. 2023), biasing the inferred [CH_3CN]/[CH_3OH] abundance ratios. Tracing back the abundances measured in the gas phase to their ice abundances in the mid-plane is therefore complicated by multiple chemical pathways and by the dust opacity in the midplane.

Finally, although less critical for methanol and methyl cyanide, different molecular binding energies (BEs) mean that species desorb at distinct temperatures, which can bias the retrieved abundance ratios. This thermal desorption behavior is further complicated because BEs are characterized by distributions rather than single discrete values (e.g., Kakkar et al. 2025, see Appendix C).

4. Conclusions

We implemented the first statistical comparison of the methyl cyanide to methanol abundance ratio in 13 comets, 24 low-mass hot corinos, and seven protoplanetary disks belonging to Class 0, Class I, and Class II stages. We list our conclusions below:

- For comets, we provided the first statistical analysis of CH_3CN abundances by investigating the sample diversity and accounting for different sources of fluctuation (e.g., dynamical types or heliocentric distances). This offered a comprehensive view of the comet population. Additionally, we compared our database with the data collected for comet 67P as observed by the ROSINA mass spectrometer on board the ESA-Rosetta mission (Le Roy et al. 2015; Rubin et al. 2019) and with recent results for the interstellar object 3I (Biver et al. 2026);
- When we compared comets to star- and planet-forming regions, we observed a strong dichotomy, with hot corinos and comets showing a statistically comparable [CH_3CN]/[CH_3OH] abundance ratio (0.0044–0.04), and disks from Class 0 to Class II revealing very different values and a large dispersion;
- We observed that the correlation of the CH_3CN and CH_3OH MRs is far weaker in comets than in hot corinos. Although this discrepancy might be a statistical artifact in part, we also noted a potential dichotomy between dynamically new and long-period comets. This trend might suggest distinct formation times and locations within the protoplanetary disk, differing post-formation thermal histories, active coma processes, or a combination of these factors.

While the consistent [CH_3CN]/[CH_3OH] abundance ratios observed between hot corinos and comets provide a compelling argument for chemical inheritance, the full evolutionary sequence indicates that planet formation involves a dramatic reshaping of material and not simple preservation.

If CH_3CN is primarily formed with CH_3OH on grain surfaces in cold environments prior to the hot corino stage, then the observed abundance ratios might reflect inherited ice chemistry from the prestellar phase. However, since CH_3CN is also produced in the gas phase following CH_3OH sublimation, the differences between hot corinos and inner disks would more strongly indicate gas-phase processing than ice inheritance. Regardless of the pathway, the reprocessed material in hot corinos and disks is expected to refreeze onto solids and become incorporated into comets. With the current database, we are unable to distinguish which scenario is more plausible. Nevertheless, since cometary and hot corino abundances match consistently, this might imply that even if significant disk-stage reprocessing occurs, the chemistry eventually resets the [CH_3CN/CH_3OH] ratio back to $\approx$0.01 prior to incorporation into comets. Finally, we must also consider that CH_3OH in disks is typically detected in the hot irradiated gas close to the star, whereas the comet-forming zone lies farther

out. Consequently, the disk gas probed by methanol observations might have undergone different chemical processing than the shielded ice reservoir at larger radii, where comets actually form.

It was essential to adopt a robust statistical approach for a more comprehensive view of the evolution of the $[CH_3CN]/[CH_3OH]$ and to identify data inconsistencies and biases that required careful review. By aggregating data from multiple hot corino surveys, for instance, we identified systematic discrepancies that are most likely related to model assumptions. These differences would have remained undetected if we had used a single source as a reference, with the risk of a biased final conclusion. Moreover, a large sample size is critical for characterizing the inherent heterogeneity of hot corinos, protoplanetary disks, and comets. Our work highlights the limitations of current datasets, but also establishes a standard for linking pristine Solar System bodies to their interstellar counterparts.

Acknowledgements. The authors thank the anonymous referee for their constructive comments and suggestions, which have significantly improved the quality of this manuscript. M. L. acknowledges the "NextGenerationEU" program, in the context of the "Piano Nazionale di Ripresa e Resilienza (PNRR)", project code SOE-0000188 ("ProDisCo – A systematic comparison between measured molecular abundances in comets and protoplanetary disks", PI: Manuela Lippi) – CUP C13C22000900006 and the INAF GO 2024 ICES: Tracking the history of ices from the cradles of planets to comets (ref. Dr. L. Podio). L.P. and Cl.Co. acknowledge financial support under the National Recovery and Resilience Plan (NRRP), Mission 4, Component 2, Investment 1.1, Call for tender No. 104 published on 2.2.2022 by the Italian Ministry of University and Research (MUR), funded by the European Union – NextGenerationEU-Project Title 2022JC2Y93 Chemical Origins: linking the fossil composition of the Solar System with the chemistry of protoplanetary disks – CUP J53D23001600006 – Grant Assignment Decree No. 962 adopted on 30.06.2023 by the Italian Ministry of Ministry of University and Research (MUR); the project ASI-Astrobiologia 2023 MIGLIORA ("Modeling Chemical Complexity", F83C23000800005); the INAF-GO 2024 fundings ICES, the INAF-GO 2023 fundings PROTOSKA ("Exploiting ALMA data to study planet forming disks: preparing the advent of SKA", C13C23000770005); the INAF Mini-Grant 2022 "Chemical Origins". C.W. acknowledges financial support from the Science and Technology Facilities Council and UK Research and Innovation (grant numbers ST/X001016/1 and MR/Z00019X/1). M.A.C. was supported by NSF grant AST-2509096 and the NASA Planetary Science Division Internal Scientist Funding Program through the Fundamental Laboratory Research work package (FLaRe). Alice S. Booth gratefully acknowledges the support by the Clay Fellowship of the Smithsonian Astrophysical Observatory, made possible by the generosity of the Clay Family.

References

Beichman, C., & Harris, S. 1981, ApJ, 245, 589
Belloche, A., Maury, A. J., Maret, S., et al. 2020, A&A, 635, A198
Bianchi, E., Codella, C., Ceccarelli, C., et al. 2019, MNRAS, 483, 1850
Biver, N., Bockelée-Morvan, D., Crovisier, J., et al. 2006, A&A, 449, 1255
Biver, N., Bockelée-Morvan, D., Colom, P., et al. 2011, A&A, 528, A142
Biver, N., Bockelée-Morvan, D., Moreno, R., et al. 2015, Sci. Adv., 1, 1500863
Biver, N., Bockelée-Morvan, D., Boissier, J., et al. 2021a, A&A, 648, A49
Biver, N., Bockelée-Morvan, D., Lis, D. C., et al. 2021b, A&A, 651, A25
Biver, N., Boissier, J., Bockelée-Morvan, D., et al. 2022, A&A, 668, A171
Biver, N., Bockelée-Morvan, D., Crovisier, J., et al. 2023, A&A, 672, A170
Biver, N., Bockelée-Morvan, D., Handzlik, B., et al. 2024a, A&A, 690, A271
Biver, N., Dello Russo, N., Opitom, C., & Rubin, M. 2024b, in Comets III, eds. K. J. Meech, M. R. Combi, D. Bockelée-Morvan, S. N. Raymond, & M. E. Zolensky, 459
Biver, N., Bockelée-Morvan, D., Moreno, R., et al. 2026, A&A, 708, L16
Bockelée-Morvan, D., Lis, D. C., Wink, J. E., et al. 2000, A&A, 353, 1101
Bockelée-Morvan, D., Crovisier, J., Mumma, M. J., & Weaver, H. A. 2004, in Comets II, eds. M. C. Festou, H. U. Keller, & H. A. Weaver (UAPress), 391
Boitard-Crépeau, L., Pantaleone, S., Ceccarelli, C., et al. 2026, MNRAS, 548, stag789
Bonev, B. P., Dello Russo, N., DiSanti, M. A., et al. 2021, PSJ, 2, 45
Booth, A. S., Leemker, M., van Dishoeck, E. F., et al. 2024a, AJ, 167, 164
Booth, A. S., Temmink, M., van Dishoeck, E. F., et al. 2024b, AJ, 167, 165
Booth, A. S., Wölfer, L., Temmink, M., et al. 2025, ApJ, 986, L9
Booth, A. S., Calahan, J., Temmink, M., et al. 2026, AJ, 171, 128
Brasser, R., & Morbidelli, A. 2013, Icarus, 225, 40
Calahan, J. K., Bergin, E. A., Bosman, A. D., et al. 2023, Nat. Astron., 7, 49
Calahan, J. K., Bergin, E. A., van't Hoff, M., et al. 2024, ApJ, 975, 170
Calcutt, H., Fiechter, M. R., Willis, E. R., et al. 2018, A&A, 617, A95
Carvalho, A. S., Hillenbrand, L. A., Herczeg, G. J., & France, K. 2025, ApJ, 994, L12
Ceccarelli, C., Codella, C., Balucani, N., et al. 2023, in Astronomical Society of the Pacific Conference Series, 534, Protostars and Planets VII, eds. S. Inutsuka, Y. Aikawa, T. Muto, K. Tomida, & M. Tamura, 379
Collings, M. P., Anderson, M. A., Chen, R., et al. 2004, MNRAS, 354, 1133
Cordiner, M. A., & Charnley, S. B. 2021, MNRAS, 504, 5401
Cordiner, M. A., Roth, N. X., Milam, S. N., et al. 2023, ApJ, 953, 59
Cordiner, M., Roth, N. X., Micheli, M., et al. 2026, Nature, 655, 870
Cruz-Sáenz de Miera, F., Coutens, A., Kóspál, Á., et al. 2025, A&A, 696, A18
Das, A., Sil, M., Gorai, P., Chakrabarti, S. K., & Loison, J. C. 2018, ApJS, 237, 9
Drozdovskaya, M. N., van Dishoeck, E. F., Rubin, M., Jørgensen, J. K., & Altwegg, K. 2019, MNRAS, 490, 50
Enrique-Romero, J., & Lamberts, T. 2025, A&A, 699, A235
Evans, L., Booth, A. S., Walsh, C., et al. 2025, ApJ, 982, 62
Fadul, A. M. A., Schwarz, K. R., van'T Hoff, M. L. R., et al. 2025, AJ, 169, 307
Ferrero, S., Zamirri, L., Ceccarelli, C., et al. 2020, ApJ, 904, 11
Ferrero, S., Grieco, F., Ibrahim Mohamed, A.-S., et al. 2022, MNRAS, 516, 2586
Frediani, J., De Simone, M., Testi, L., et al. 2025, A&A, 695, A78
Garrod, R. T. 2008, A&A, 491, 239
Garrod, R. T., Jin, M., Matis, K. A., et al. 2022, ApJS, 259, 1
Geppert, W. D., Vigren, E., Hamberg, M., et al. 2007, in Journal of Physics Conference Series, Vol. 88, Journal of Physics Conference Series (IOP), 012068
Giani, L., Ceccarelli, C., Mancini, L., et al. 2023, MNRAS, 526, 4535
Giannetti, A., Leurini, S., Wyrowski, F., et al. 2017, A&A, 603, A33
Gomes, R., Levison, H. F., Tsiganis, K., & Morbidelli, A. 2005, Nature, 435, 466
Hasegawa, T. I., & Herbst, E. 1993, MNRAS, 263, 589
Herbst, E. 1985, ApJ, 292, 484
Ilee, J. D., Walsh, C., & Calahan, J. K. 2026, AJ, 171, 3
Jeong, J.-H., Lee, J.-E., Lee, S., et al. 2025, ApJS, 276, 49
Jørgensen, J. K., van der Wiel, M. H. D., Coutens, A., et al. 2016, A&A, 595, A117
Jørgensen, J. K., Müller, H. S. P., Calcutt, H., et al. 2018, A&A, 620, A170
Kakkar, H., Martínez-Bachs, B., Ceccarelli, C., Ugliengo, P., & Rimola, A. 2025, ApJ, 993, 184
Klippenstein, S. J. 1996, J. Chem. Phys., 104, 5437
Kopatskaia, E. N. 1984, Astrofizika, 20, 263
Le Roy, L., Altwegg, K., Balsiger, H., et al. 2015, A&A, 583, A1
Lee, J.-E., Lee, S., Baek, G., et al. 2019, Nat. Astron., 3, 314
Lippi, M., Podio, L., Codella, C., et al. 2024, ApJ, 970, L5
Loomis, R. A., Cleeves, L. I., Öberg, K. I., et al. 2018, ApJ, 859, 131
Manigand, S., Jørgensen, J. K., Calcutt, H., et al. 2020, A&A, 635, A48
Maret, S., Hily-Blant, P., Pety, J., Bardeau, S., & Reynier, E. 2011, A&A, 526, A47
Minissale, M., Aikawa, Y., Bergin, E., et al. 2022, ACS ESC, 6, 597
Mumma, M. J., & Charnley, S. B. 2011, ARA&A, 49, 471
Nazari, P., Rocha, W. R. M., Rubinstein, A. E., et al. 2024, A&A, 686, A71
Öberg, K. I., Guzmán, V. V., Furuya, K., et al. 2015, Nature, 520, 198
Opitom, C., Manfroid, J., Hutsemékers, D., et al. 2026, Nat. Astron., https://doi.org/10.1038/s41550-026-02921-7
Ortiz-León, G. N., Loinard, L., Dzib, S. A., et al. 2018a, ApJ, 865, 73
Ortiz-León, G. N., Loinard, L., Dzib, S. A., et al. 2018b, ApJ, 869, L33
Rachid, M. G., Rocha, W. R. M., & Linnartz, H. 2022, A&A, 665, A89
Rubin, M., Altwegg, K., Balsiger, H., et al. 2019, MNRAS, 489, 594
van't Hoff, M. L. R., Bergin, E. A., Riley, P., et al. 2024, ApJ, 970, 138
Wakelam, V., Loison, J. C., Mereau, R., & Ruaud, M. 2017, Mol.Astr., 6, 22
Walsh, C., Loomis, R. A., Öberg, K. I., et al. 2016, ApJ, 823, L10
Willacy, K., Majumdar, L., Bonev, B., et al. 2025, AJ, 170, 312
Yamato, Y., Notsu, S., Aikawa, Y., et al. 2024, AJ, 167, 66
Yang, Y.-L., Sakai, N., Zhang, Y., et al. 2021, ApJ, 910, 20
Zucker, C., Speagle, J. S., Schlafly, E. F., et al. 2019, ApJ, 879, 125

Appendix A: Molecular abundance statistics for comets

In Table A.1 we list the production rates as reported in the literature for the sample of comets we used for our research. To evaluate differences between the various samples and subsamples, we employed a Kolmogorov-Smirnov (KS) test which detects any difference in shape, spread, or median and a Wilcoxon-Mann-Whitney (WMW) test which compares ranks/medians. These two tests are nonparametric and do not assume a particular distribution of the data. The Kolmogorov-Smirnov test is less sensitive to small samples ($N < 20$) than the Wilcoxon-Mann-Whitney one, still in our analysis these two approaches give consistent results (see Table A.3).

Appendix B: Differences between the CALYPSO and PEACHES surveys

Given that values reported in the CALYPSO survey (Belloche et al. 2020) are consistently higher than those in PEACHES (Yang et al. 2021), we investigated for potential systematic errors. Figure B.1 and Table B.1 compare the results for the six common sources: L1448-2A, L1448-C, SVS-13A, IRAS-2A1, IRAS-4A2, and IRAS-4B1. We find that estimated abundance ratios for CH_3CN generally exhibit larger discrepancies than those for CH_3OH. Specifically, the relative difference[3] for CH_3CN ranges from $\approx$ 18 to 85%, compared to $\approx$ 11 to 65 % for CH_3OH, with the notable exception of L1448-2A, which shows a difference of 300% in the estimated column densities of methanol. Overall, the discrepancies in the $[CH_3CN]/[CH_3OH]$ ratio are nonuniform across the sample. The ratios are only consistent within 20% ($\Delta \leq 20\%$) for IRAS-4B1 and IRAS-4A2. The largest divergence occurs in L1448-2A ($\Delta \approx -0.04$), while the smallest is observed in IRAS-4A2 ($\Delta \approx -0.002$). Finally, we note that for IRAS-2A1, IRAS-4A2, and IRAS-4B1, the CALYPSO $[CH_3CN]/[CH_3OH]$ values are treated as upper limits, as they were derived using rotational temperatures distinct from those of methanol (see main text).

Appendix C: Methanol and methyl cyanide binding energy distributions

Adopting a Binding Energy (BE) distribution rather than a single discrete value is fundamental to modeling the gradual thermal desorption observed in star- and planet-forming environments. BEs can be evaluated using theoretical quantum-mechanical methods, and laboratory experiments (see e.g., Minissale et al. 2022; Ceccarelli et al. 2023; Collings et al. 2004). These investigations reveal that each species is associated with a BEs spectrum rather than a single value, due to the sensitivity of the adsorbate–surface interaction to the specific adsorption site. The orientation of the adsorbed molecule is also a key parameter. Over time, the reliability of computational models has been enhanced by employing increasingly complex substrates, ranging from small clusters of water molecules (up to six, Wakelam et al. 2017; Das et al. 2018) to amorphous water ice structures (Ferrero et al. 2020, 2022). So far, the BE distribution of methanol and methyl cyanide has been computed only for a substrate of amorphous water ice (Kakkar et al. 2025). From their calculations it is possible to notice that while the median BEs of methyl cyanide is smaller compared to that of methanol, its overall distribution is larger (see Fig. C.1), meaning these two molecules can desorb in different amounts at each disk radii, thus producing slightly skewed abundance ratios. On the other hand, the first one or two layers of methanol and methyl cyanide frozen directly adsorbed on the silicate and carbonaceous surfaces of the interstellar grains would result in a definitively larger BE, as it is the case for water molecules, the only case where this calculations have been carried out (Boitard-Crépeau et al. 2026). However, it is unlikely that an significant fraction of methanol and methyl cyanide is frozen directly on the silicate and carbonaceous surfaces, because these species are formed later than frozen water, the major component of interstellar ices, and, therefore, not in the first ice layers. Besides, their BEs are similar to those of water, so that they would sublimate with the latter.

[3] We define the relative difference as: $|100 * (Measure_{CALYPSO} - Measure_{PEACHES})/(Measure_{CALYPSO})|$

Table A.1: Production rates of CH_3CN, CH_3OH, and H_2O in Solar System comets, from ground-based observations.

Comet	Date dd.mm.aa	$R_h^{(a)}$ (au)	CH_3CN 10^{25} mol/s	CH_3OH 10^{25} mol/s	H_2O 10^{28} mol/s	Refs
21P/Giacobini-Zinner	14-18.09.18	1.02	0.78 ± 0.10	53.9 ± 3.3	3.0 ± 0.3	(1)
46P/Wirtanen	12.12.18	1.06	0.22 ± 0.04	34.7 ± 0.6	0.80 ± 0.08	(2)
	13.12.18	1.06	0.22 ± 0.05	30.0 ± 2.0	0.80 ± 0.08	(2)
	15.12.18	1.06	0.16 ± 0.03	27.3 ± 1.8	0.80 ± 0.08	(2)
	16.12.18	1.06	0.17 ± 0.02	28.5 ± 0.8	0.80 ± 0.08	(2)
	17.12.18	1.06	0.16 ± 0.02	25.3 ± 0.3	0.80 ± 0.08	(2)
	18.12.18	1.06	0.12 ± 0.02	22.9 ± 0.8	0.80 ± 0.08	(2)
	25.12.18	1.07	0.10 ± 0.02	18.4 ± 1.4	0.80 ± 0.08	(2)
46P/Wirtanen	02-07.12.18	1.10	0.08 ± 0.01	18.9 ± 0.7	0.7 ± 0.1	(3)
67P/C.G.	12-16.11.21	1.22	0.20 ± 0.04	14.4 ± 0.7	1.19 ± 0.44	(4)
153P/Ikeya–Zhang	20.03.02	0.51	17 ± 6	1040 ± 270	70 ± 7	(5)
	29.04.02	1.1	2.1 ± 0.4	380 ± 40	16 ± 2	(5)
C/1995 O1 (Hale-Bopp)	01.02-04.97	1.0	200 ± 20	24000 ± 2400	1000 ± 100	(6)
C/2000 WM1 (LINEAR)	25.11.01	1.33	0.4 ± 0.1	30 ± 3	2.5 ± 0.3	(5)
C/2001 A2 (LINEAR)	08-09.07.01	1.16	1.1 ± 0.4	112 ± 16	4.0 ± 0.4	(5)
C/2002 X5 (Kudo-Fujikawa)	26.01.03	0.2	56 ± 22	8410 ± 82	350 ± 40	(7)
C/2006 P1 (McNaught)	17.01.07	0.26	106 ± 40	6450 ± 770	1000 ± 200	(7)
C/2014 Q2 (Lovejoy)	13-25.01.15	1.3	8.0 ± 1.7	1300 ± 200	55 ± 2	(8)
C/2020 F3 (NEOWISE)	22.07.20	0.62	6.6 ± 2.0	1550 ± 500	60 ± 6	(9)
	25.07.20	0.69	2.2 ± 2.3	970 ± 50	35 ± 4	(9)
	26.07.20	0.71	5.5 ± 1.5	930 ± 40	35 ± 4	(9)
C/2021 A1 (Leonard)	13.12.21	0.77	0.59 ± 0.06	38 ± 1	4.0 ± 0.4	(10)
C/2022 E3 (ZTF)	04.02.23	1.17	0.87 ± 0.05	89 ± 1	5.0 ± 0.5	(10)
	05.02.23	1.18	0.84 ± 0.06	87 ± 3	5.0 ± 0.5	(10)
	06.02.23	1.18	0.62 ± 0.17	79.5 ± 0.9	5.0 ± 0.5	(10)

Notes. [(a)]Heliocentric distance at the time of observations.
References. (1) Biver et al. (2021b); (2) Biver et al. (2021a); (3) Cordiner et al. (2023); (4) Biver et al. (2023); (5) Biver et al. (2006); (6) Bockelée-Morvan et al. (2000); (7) Biver et al. (2011); (8) Biver et al. (2015); (9) Biver et al. (2022); (10) Biver et al. (2024a).

Table A.2: Mixing Ratios (relative to water) statistics of CH_3CN for the comets considered in this work (see Table 1).

Statistic	All	$R_h < 1$	$R_h > 1$	DN	LP	JF	67P
Median	0.016	0.014	0.017	0.015	0.016	0.017	0.006
Std	0.005	0.003	0.005	0.004	0.005	0.005	0.005
25th	0.014	0.010	0.015	0.013	0.015	0.016	0.006
75th	0.017	0.016	0.019	0.016	0.019	0.019	0.011
Max	0.028	0.016	0.028	0.017	0.028	0.026	0.016
Min	0.008	0.008	0.011	0.008	0.011	0.011	0.006
Sample Size	14	4	10	4	6	4	3

Table A.3: Statistical KS and WMW tests for comparing CH_3CN MRs in different comets subgroups (see Table 1).

Sample 1	Sample 2	KS[(a)]	MW[(b)]
$R_h < 1$	$R_h > 1$	0.1878	0.1059
OC	LP	0.9238	0.4762
OC	JF	0.7714	0.3429
LP	JF	0.6952	0.9143
All	67P	**0.0167**	**0.0167**

Notes. [(a)]p-values calculated from KS test statistics[(b)]p-values calculated from WMW test statistics.Values in bold indicate statistically significant p-values, i.e., statistically significant differences between Sample 1 and Sample 2.

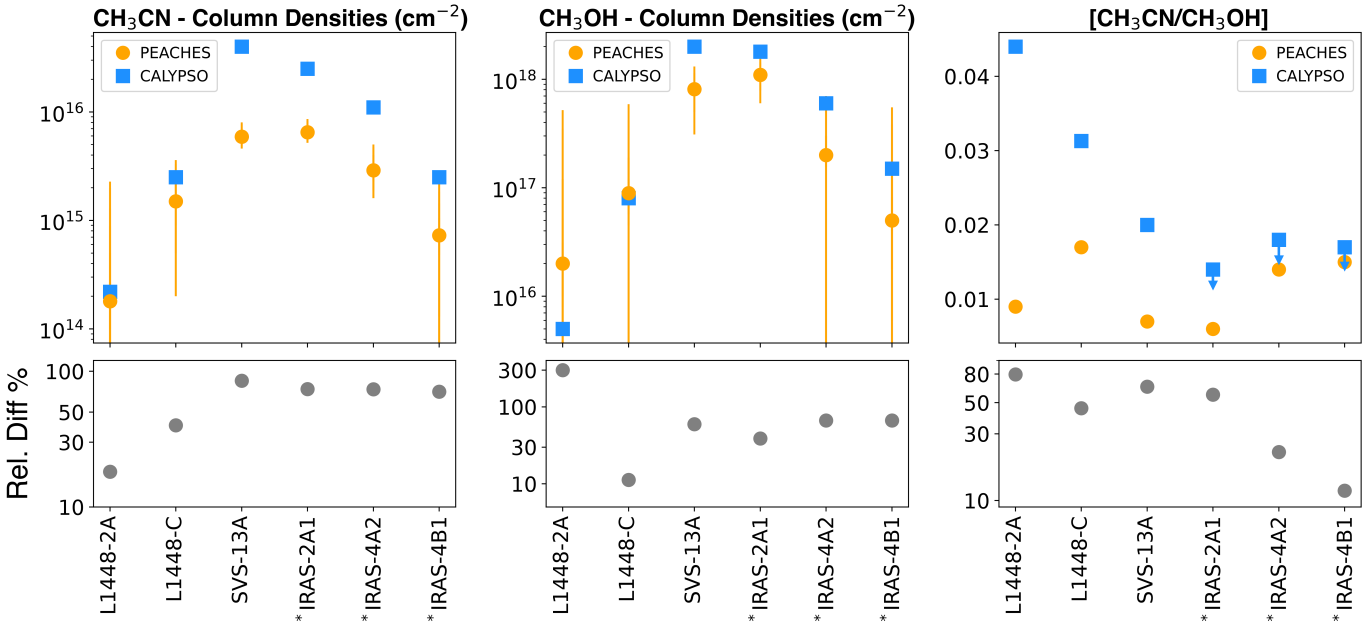


Fig. B.1: Comparison between the two surveys ALMA PEACHES in orange (Yang et al. 2021) and IRAM PdBI CALYPSO in blue (Belloche et al. 2020), for the same observed sources. In the top panels we show the absolute differences in CH_3CN (left), CH_3OH (middle) and $[CH_3CN]/[CH_3OH]$ ratio (right), while in the bottom panels we show the corresponding relative differences in %. Data from the CALYPSO survey do not have an error estimate, so in the Figure only the PEACHES ones are reported.

Table B.1: Comparison of estimated column densities for CH_3CN and CH_3OH, and for the $[CH_3CN]/[CH_3OH]$ abundance ratios in the ALMA PEACHES (Yang et al. 2021) and IRAM PdBI CALYPSO (Belloche et al. 2020) surveys.

	CH_3CN (10^{14} cm^{-2})			CH_3OH (10^{16} cm^{-2})			$[CH_3CN]/[CH_3OH]$		
Sources	PEACHES	CALYPSO	Rel. Diff (%)	PEACHES	CALYPSO	Rel. Diff (%)	PEACHES	CALYPSO	Rel. Diff (%)
L1448-2A	$1.8^{+0.9}_{-0.8}$	2.2	18	$2^{+1.1}_{-1.2}$	0.5	300	0.009	0.044	80
L1448-C	15^{+7}_{-6}	25	40	$8.9^{+3.2}_{-4.4}$	8	11	0.017	0.031	46
IRAS-2A1	59^{18}_{-13}	400	85	81^{50}_{-31}	200	60	0.006	0.014	57
SVS-13A	65^{+21}_{-13}	250	74	110^{+10}_{-50}	180	65	0.007	0.02	65
IRAS-4A2	29^{+11}_{-10}	110	74	20^{+10}_{-1}	60	67	0.014	0.018	22
IRAS-4B1	$7.3^{+3.2}_{-2.5}$	25	72	$5^{+3.3}_{-3.2}$	15	67	0.015	0.017	12

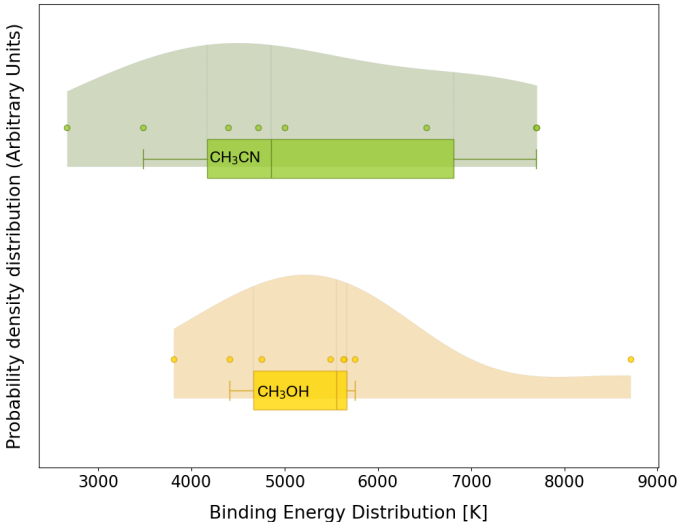


Fig. C.1: Binding energy distribution of methanol (yellow box plot on the bottom) and methyl cyanide (green box plot on the top), obtained using the BEs calculated in Kakkar et al. (2025) for different adsorption sites of the amorphous water ice model. The colored shape around each box plot represents the probability density distribution.